Chapter

Excitation of Wakefields in Graphene Layers: PIC Simulations vs. Hydrodynamic Model

Pablo Martín-Luna, Juan Rodríguez-Pérez, Alexandre Bonatto, Cristian Bontoiu, Guoxing Xia and Javier Resta-López

Abstract

The interaction between charged particles and graphene layers can lead to the collective oscillation of free electrons within the graphene shell, resulting in electromagnetic modes. These plasmonic modes offer strong potential for enabling ultra-high acceleration gradients in particle acceleration systems. Their behavior can be effectively explored using both particle-based simulations and analytical modeling approaches. This chapter begins by introducing the linearized hydrodynamic model, which provides an analytical framework for describing the plasmonic modes excited by a point-like charge interacting with graphene layers. In this model, the free electron gas at the layers is treated as a plasma, governed by the linearized continuity and momentum equations with different solid-state properties such as the interactions with acoustic modes, a quantum correction, and the scattering due to ionic-lattice charges. Subsequently, the plasmonic excitations obtained from the hydrodynamic model are compared with those derived from PIC simulations performed with the WarpX code. While the hydrodynamic model offers analytical insight into the excitation of plasmonic modes, the PIC simulations provide a more comprehensive treatment of nonlinear and collective effects. The comparison reveals consistent trends in mode structure but highlights differences in amplitude and spatial results. The analysis highlights key similarities, distinctions, and constraints between the two approaches. Overall, the study provides meaningful insight into how graphene layers could be harnessed to improve particle acceleration methods, potentially driving future innovations in high-energy physics and related disciplines.

Keywords: linearized hydrodynamic model, particle-in-cell (PIC) simulations, graphene layers, wakefield excitation, plasmonics, particle acceleration

1. Introduction

Particle accelerators are indispensable tools across multiple sectors, including scientific research, industrial applications, and national security [1, 2]. They have been at the forefront of high-energy physics studies for over half a century and serve as critical components in technologies such as synchrotron radiation sources and free

electron lasers [3, 4]. Additionally, their role in medicine is well-established, particularly in cancer treatments such as radiotherapy and hadrontherapy [5]. Despite their advantages, conventional accelerators that rely on radio frequency (RF) systems face limitations, with achievable gradients capped at approximately 100 MV/m due to surface RF breakdown [6, 7]. To address these constraints, researchers are exploring innovative alternatives, including dielectric laser accelerators and wakefield accelerators [8–12], as well as plasma-based acceleration methods [13–17], which have the potential to overcome the current technological limitations and unlock new opportunities in particle acceleration.

Tajima and Cavenago [18] in 1987 and Chen and Noble [19, 20] in the 1990s introduced the concept of solid-state wakefield acceleration, leveraging the ion lattice structure of crystals as a promising approach to achieve acceleration gradients on the order of several TV/m. In this method, longitudinal wakefields could be excited within the crystal by either X-rays or charged particle bunches traveling through it. Despite its potential, this technique is limited due to the angstrom-scale channels present in natural crystals, which restricts beam intensity acceptance and contributes to high dechanneling rates. Overcoming these technical challenges is essential to unlocking the full capabilities of crystal-based solid-state wakefield acceleration.

In this context, carbon-based nanostructures are undergoing extensive research as the promising candidates for wakefield acceleration [21–27]. Their unique design, with broader apertures compared to crystals, provides a significant advantage by addressing the angstrom-scale constraint inherent to natural crystals, paving the way for more efficient acceleration mechanisms.

In particular, since the discovery of graphene by Novoselov et al. in 2004 [28], these carbon nanostructures have garnered extensive attention for its potential applications across numerous fields, including energy storage, biotechnology, medical science, electronics, optics, and THz technology. Their remarkable electrical, thermo-mechanical, and optical characteristics have made them a highly versatile material for innovative technological and scientific advancements [29]. As a result, both the vibrational [30–32] and electronic properties [33–35] of graphene layers have been widely explored using both theoretical approaches and experimental techniques.

Wakefields in graphene can be generated by the collective oscillation of the free electron gas confined to the layer surface, commonly known as plasmons, which are induced by passage of the driving bunch [26, 36]. The study of plasmon excitations on graphene surfaces has attracted significant attention, both experimentally [37–39] and theoretically [36, 40–47]. Experimentally, electron energy loss spectroscopy (EELS) has been employed to study these electronic excitations in both single-layer and multilayer graphene. In particular, Kinyanjui et al. [37] discovered that π plasmons in free-standing graphene monolayers exhibit a linear dispersion, in contrast to the parabolic behavior observed in graphite, an observation that aligns with theoretical predictions for a two-dimensional Dirac electron gas. Wachsmuth et al. [38] explored the collective electronic excitations in free-standing single-layer graphene and found that, for finite momentum transfers, the experimental electron energy-loss spectra agree well with time-dependent density-functional theory (DFT) calculations—provided that crystal local-field effects are considered. Regarding the multilayer graphene, Eberlein et al. [39] showed that while monolayer graphene lacks the $\sim$4.6 eV out-of-plane plasmon seen in graphite, this mode reappears in bilayer and trilayer graphene, revealing how plasmonic features, including peak positions and amplitudes, evolve with layer number and interlayer separation.

On the other hand, theoretical investigations have employed various methodologies, including a kinetic model [40], the random phase approximation (RPA) [41], molecular dynamics simulations [42], DFT studies, and hydrodynamic models [36, 43–47]. For instance, the kinetic model developed by Fermanian Kammerer and Méhats [40] captures the transport of electrons in a graphene layer by solving a Boltzmann-type equation, proposing an algorithmic realization and giving analytic justification of the model. Allison et al. [41] used the RPA to study stopping and image forces on charges near doped graphene. Their results highlight the role of interband excitations at high speeds and complex friction behavior at low speeds. Loche et al. [42] used molecular dynamics to study hydrated ion interactions with graphene surfaces. They found that non-electrostatic repulsion and van der Waals attraction dominate at short and intermediate distances. Crucially, nonlinear dielectric effects emerge near the surface, challenging standard electrostatic models. Polini et al. [48] developed a Kohn-Sham-Dirac DFT framework for graphene, showing that exchange-correlation effects increase with carrier density and significantly influence nonlinear screening, particularly in the presence of charged impurities and electron-hole puddles. Shu et al. [49] used time-dependent DFT to study high-frequency plasmons in nitrogen-doped graphene nanostructures. They found enhanced optical absorption and tunable plasmon resonances in the visible and ultraviolet range, offering a promising route for nanoscale plasmonic devices beyond the terahertz regime. Regarding the hydrodynamic models, Radović et al. [36, 43, 44] employed them, both one- and two-fluid, to investigate the interaction of fast charged particles and dipoles with graphene and supported 2D electron gases. Their studies revealed the emergence of dynamic polarization forces, directional image and stopping forces, and velocity-dependent torques on dipoles. They also demonstrated the formation of oscillatory wake effects in the induced charge density and potential when particle speeds exceeded plasmon excitation thresholds. These findings highlight the rich collective response of graphene-like systems to external perturbations. Li et al. [45] used a quantum hydrodynamic model to study the charged particle interactions with double-layered 2D electron gases. They found oscillatory wake effects in the induced potential and double peaks in stopping and image forces due to plasmon hybridization. These results highlight key differences compared to single-layer systems. Borka et al. [46] developed a dielectric response model, using a 2D two-fluid hydrodynamic model, for multilayer graphene and studied energy loss of fast electrons. They found that total energy loss decreases with increasing kinetic energy and scales with the number of layers. Plasmon peak shifts were also observed at lower energies, revealing layer-dependent polarization effects. Chaves et al. [47] used a hydrodynamic model to study plasmonic wakes induced by moving charges near graphene. They identified a transition from Mach-type to Kelvin-type wakes and introduced a tunable Froude number. Their findings suggest new mechanisms for generating and controlling graphene plasmons.

Alternatively, plasmon excitations can be characterized using particle simulations that account for particle motion. Within this framework, particle-in-cell (PIC) codes have proven to be a powerful tool for modeling these excitations, albeit with certain limitations [50]. From this point onward, we highlight a few relevant studies that employed PIC approaches to investigate the plasmonic and electronic properties of two-dimensional materials such as graphene and related systems. In 2019, Sangwan et al. [51] investigated the interaction of a 10 PW laser with a fully ionized planar carbon target using the open-source PIC code EPOCH [52]. Their simulations demonstrated that carbon ions can be accelerated to energies on the order of GeV for a target

thickness of approximately 120 nm, indicating that this configuration is suitable for producing C^{6+} ions for hadrontherapy applications. In 2023, Bontoiu et al. [22] employed the PIConGPU [53] code to simulate laser-driven electron acceleration in ionized graphene layers, uncovering a novel collective self-injection mechanism, referred to as catapult acceleration, which arises from edge plasma oscillations and enables the generation of field gradients reaching several TV/m. More recently, in 2025, Lei et al. [54] have demonstrated, through 3D particle-in-cell simulations performed in WarpX [55], the feasibility of using nanostructured carbon nanotube forests for ultra-compact plasma-based accelerators driven by relativistic electron beams, revealing two efficient mechanisms (surface plasmon leakage and bubble wakefields) that enable PeV-level particle acceleration and are compatible with the current experimental capabilities.

Recent advances in hydrodynamic modeling have demonstrated the effectiveness of these approaches in capturing nonlocal and quantum effects in plasmonic systems, particularly at nanometric scales. For instance, Ciracì et al. [56] formulated a macroscopic hydrodynamic model that incorporates essential quantum mechanical features of electron behavior in metals, including the influence of nonlocal response and boundary conditions. In this context, Toscano et al. [57] developed a self-consistent hydrodynamic model that accounts for electron spill-out effects, enabling the accurate prediction of size-dependent surface resonance shifts in metallic nanostructures. Their results show good agreement with both experimental data and more advanced quantum methods, while maintaining significantly lower computational cost.

Given the demonstrated applicability and predictive accuracy of the linearized hydrodynamic model (LHM) in capturing key plasmonic and electronic phenomena at the nanoscale, the motivation of the present work is to compare the excited wakefields predicted by the LHM [26] with PIC simulations performed with WarpX, discussing the similarities and discrepancies between both approximations.

This chapter is organized as follows. Section 2 examines the LHM, presenting general formulations for the longitudinal and transverse wakefields induced by the interaction of a point-like charged particle moving parallel to graphene layers. Section 3 describes the model that we consider in the PIC simulations for modeling the graphene layers. Then, Section 4 compares the results obtained from the simulations with the LHM, discussing the similarities and limitations in Section 5. Finally, Section 6 provides a summary of the key findings of this study.

2. Linearized hydrodynamic model

In this study, a linearized hydrodynamic theory is utilized to examine the excitations caused by a single-charged particle in graphene layers [26]. This model assumes N graphene layers positioned parallel to each other on planes $y_1 \leq y_2 \leq \ldots \leq y_N$, with each layer considered to have a negligible thickness. The delocalized electrons associated with carbon ions are treated as a two-dimensional free electron gas (Fermi gas), constrained to the surface of the jth layer with an initial uniform surface charge density n_{0j}.

We analyze the motion of a point-like charge Q traveling with a constant velocity v along the z-axis (see **Figure 1**). At any time t, the position of the moving charge is $\mathbf{r}_0(t) = (x_0, y_0, vt)$. The uniform electron gas on each layer, which will be perturbed by the interaction with the driving charge Q, is modeled as a charged fluid. This fluid is characterized by a velocity field $\mathbf{u}_j(\mathbf{r}_j, t)$ and a surface charge density $n(\mathbf{r}_j, t)$, expressed as $n_{0j} + n_j(\mathbf{r}_j, t)$. Here, $\mathbf{r}_j = \left(x, y_j, z\right)$ refers to a specific point on the jth

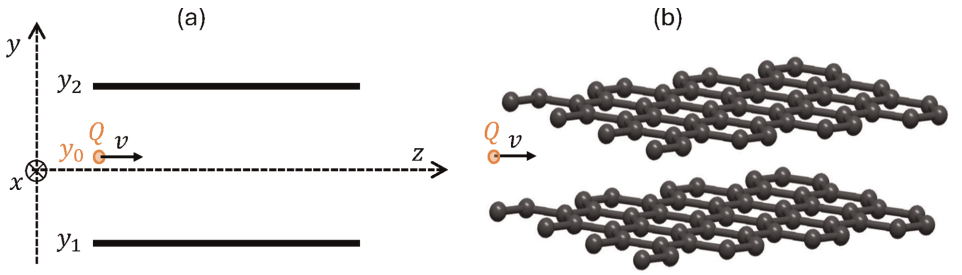

Figure 1.
(a) Scheme of the considered charge Q traveling parallel to the z-axis in the considered system composed of $N = 2$ graphene layers. (b) Schematic model of the hexagonal lattice of two graphene layers.

layer, and $n_j(\mathbf{r}_j, t)$ represents the perturbed density per unit area. Under the linearized hydrodynamic framework, it is assumed that both the perturbed densities n_j and the velocity fields $\mathbf{u}_j$ are small perturbations. Moreover, since the electronic fluid is confined to each graphene layer, the normal component of the velocity fields $\mathbf{u}_j$ is zero on the graphene surfaces. Additionally, given that the motion of carbon ions is much slower compared to that of electrons due to their significantly larger mass, ionic motion can be disregarded when analyzing wakefield dynamics [58, 59].

In this framework, the electronic excitations on graphene layers are governed by the continuity equation

$$\frac{\partial n_j(\mathbf{r}_j, t)}{\partial t} + n_{0j} \nabla_j \cdot \mathbf{u}_j(\mathbf{r}_j, t) = 0, \tag{1}$$

and the momentum-balance equation of the electron fluid at each layer

$$\frac{\partial \mathbf{u}_j(\mathbf{r}_j, t)}{\partial t} = \nabla_j \Phi(\mathbf{r}_j, t) - \frac{\alpha_j}{n_{0j}} \nabla_j n_j(\mathbf{r}_j, t) + \frac{\beta}{n_{0j}} \nabla_j \left[\nabla_j^2 n_j(\mathbf{r}_j, t) \right] - \gamma_j \mathbf{u}_j(\mathbf{r}_j, t). \tag{2}$$

In these equations, only the first-order terms in n_j and $\mathbf{u}_j$ are considered. The equations utilize the position vector $\mathbf{r} = (x, y, z)$ and the differential operator $\nabla_j = \hat{\mathbf{x}} \frac{\partial}{\partial x} + \hat{\mathbf{z}} \frac{\partial}{\partial z}$, which operates exclusively within the tangential plane of the jth graphene layer. Eq. (2) accounts for four distinct contributions. The initial term on the right-hand side describes the force acting on the electrons of the jth graphene layer, which results from the tangential electric field component induced by the moving charge Q and the associated perturbed densities. Here, Φ represents the electric scalar potential. The second term considers the potential interactions with acoustic modes, introducing the parameter $\alpha_j = v_{F_j}^2/2$, where $v_{F_j} = (2\pi n_{0j})^{1/2}$ is the Fermi velocity at the jth layer. The third contribution corresponds to a quantum correction captured by the parameter $\beta = \frac{1}{4}$. This correction emerges from the Von Weizsacker gradient term in the equilibrium kinetic energy functional of the electron fluid [60], reflecting single-electron excitations in the gas. The final component represents a frictional force arising from electron scattering due to ionic-lattice charges, with γ_j as the damping coefficient for the jth layer. This coefficient can also serve as a phenomenological parameter to describe the widening of plasmon resonance in the excitation spectra of various materials [61].

Eqs. (1) and (2) are interconnected through the Poisson's equation in free space. The overall electric potential Φ is expressed as the sum of two components: $\Phi = \Phi_0 + \Phi_{\text{ind}}$. The term $\Phi_0 = \frac{Q}{\|\mathbf{r}-\mathbf{r}_0\|}$ represents the Coulomb potential originating from the driving charge Q. In contrast, Φ_{ind} refers to the potential generated as a result of the perturbations induced in the electron fluids:

$$\Phi_{\text{ind}} = \sum_{j=1}^{N} \Phi_j, \quad \Phi_j(\mathbf{r},t) = -\int \mathrm{d}x'\mathrm{d}z' \frac{n_j\left(\mathbf{r}_j', t\right)}{\left\|\mathbf{r}-\mathbf{r}_j'\right\|}, \tag{3}$$

where Φ_j is the electric potential created by the jth layer and $\mathbf{r}_j' = \left(x', y_j, z'\right)$ are the coordinates of a general point at the surface of the jth layer.

The LHM can be solved by applying a Fourier transform to the spatial coordinates in the xz-plane, $\mathbf{R} = (x,z) \rightarrow \mathbf{k} = (k_x, k_z)$, as well as to the temporal variable, $t \rightarrow \omega$. This transformation is expressed mathematically as:

$$A(\mathbf{R}, y, t) = \frac{1}{(2\pi)^3} \int \tilde{A}(\mathbf{k}, y, \omega) e^{-i(\omega t - \mathbf{k}\cdot\mathbf{R})} \mathrm{d}^2\mathbf{k}\mathrm{d}\omega. \tag{4}$$

The Fourier transform of the electric potential generated by the moving charge, $\tilde{\Phi}_0$, and the induced electric potential due to the graphene layers, $\tilde{\Phi}_{\text{ind}}$, can be expressed, respectively, as:

$$\tilde{\Phi}_0(\mathbf{k}, y, \omega) = \frac{(2\pi)^2 Q \delta(\omega - \mathbf{k}\cdot\mathbf{v})}{k} e^{-k|y-y_0|}, \tag{5}$$

$$\tilde{\Phi}_{\text{ind}}(\mathbf{k}, y, \omega) = -\sum_{j=1}^{N} \frac{2\pi}{k} \tilde{n}_j(\mathbf{k}, \omega) e^{-k|y-y_j|}, \tag{6}$$

where we have defined $k = \sqrt{k_x^2 + k_z^2}$. By using the continuity equation to substitute and remove $\mathbf{u}_j$ in Eq. (2), and applying the Fourier transform as defined in Eq. (4), the perturbed densities in Fourier space are connected through a system of N coupled linear equations:

$$S_j(\mathbf{k}, \omega)\tilde{n}_j(\mathbf{k}, \omega) - \sum_{l=1}^{N} G_{jl}(\mathbf{k})\tilde{n}_l(\mathbf{k}, \omega) = B_j(\mathbf{k}, \omega), \tag{7}$$

where we have defined the following functions:

$$S_j(\mathbf{k}, \omega) = \omega\left(\omega + i\gamma_j\right) - \alpha_j k^2 - \beta k^4, \tag{8}$$

$$G_{jl}(\mathbf{k}) = 2\pi n_{0j} k e^{-k|y_j - y_l|}, \tag{9}$$

$$B_j(\mathbf{k}, \omega) = -n_{0j} k^2 \tilde{\Phi}_0\left(\mathbf{k}, y_j, \omega\right). \tag{10}$$

It is important to highlight that Eq. (7) can be reformulated into a matrix representation:

$$M\vec{\tilde{n}} = \vec{B}, \qquad M_{jj} = S_j - G_{jj}, \quad M_{ij} = -G_{ij} \quad (i \neq j). \tag{11}$$

Consequently, the resonant frequencies of the collective modes in the electron fluids are derived by solving the eigenvalue equation $\det(M) = 0$, under the condition $\gamma_j = 0$. After determining $\tilde{n}_j$ by solving Eq. (7), the perturbed charge densities and the resulting electric potential are computed using the Fourier transform definition, Eq. (4). Specifically, by exploiting the symmetry characteristics of the real and imaginary components of $\tilde{n}_j$ with respect to $\mathbf{k}$, the perturbed charge densities and the induced electric potential can be formally expressed as:

$$n_j(\mathbf{R}, y, t) = \frac{4}{(2\pi)^3} \int_0^\infty \int_0^\infty \mathrm{Re}\left[\tilde{n}_j(\mathbf{k}, y, k_z v) e^{ik_z \zeta}\right] \cos(k_x x) dk_x dk_z, \tag{12}$$

$$\Phi_{\mathrm{ind}}(\mathbf{R}, y, t) = \frac{4}{(2\pi)^3} \int_0^\infty \int_0^\infty \mathrm{Re}\left[\tilde{\Phi}_{\mathrm{ind}}(\mathbf{k}, y, k_z v) e^{ik_z \zeta}\right] \cos(k_x x) dk_x dk_z, \tag{13}$$

where the comoving coordinate $\zeta = z - vt$ is defined. Finally, the induced wakefields are obtained by evaluating the corresponding partial derivatives of the electric potential:

$$W_x(\mathbf{R}, y, t) = -\frac{\partial \Phi_{\mathrm{ind}}}{\partial x}, \quad W_y(\mathbf{R}, y, t) = -\frac{\partial \Phi_{\mathrm{ind}}}{\partial y}, \quad W_z(\mathbf{R}, y, t) = -\frac{\partial \Phi_{\mathrm{ind}}}{\partial z}. \tag{14}$$

3. PIC simulations

PIC simulations are widely employed to model plasma behavior, with a particular focus on the self-consistent dynamics of charged particles and electromagnetic fields [50]. Traditionally, the medium in PIC simulations is represented as a free electron gas accompanied by a neutralizing ionic background. However, contemporary PIC codes increasingly incorporate ionization models, such as the Ammosov-Delone-Krainov (ADK) model [62], enabling the simulation of ionizable atoms. This enhancement provides a more dynamic and realistic depiction of the medium, especially in scenarios where ionization plays a crucial role, such as high-intensity laser-plasma interactions [63].

These simulations begin with electrons randomly positioned to match a prescribed density profile. At every time increment, Maxwell's equations are solved to obtain the electromagnetic fields, which then guide the motion of each electron *via* the Newton-Lorentz equation. Notably, the movement of electrons induces localized currents that modify the fields in the next iteration. As a result, PIC codes are capable of tracking the trajectories of individual electrons dynamically over time.

Due to their versatility, PIC simulations can be computationally intensive. To mitigate this challenge, macroparticles, representing multiple electrons or positive ions, are often employed. Conventional PIC methods, however, are not well-suited for incorporating solid-state effects, such as lattice interactions and inter-band transitions. Additionally, certain complex physical phenomena, such as collisional effects, are frequently neglected due to their significant computational expense [50]. Nevertheless, PIC codes are highly effective for modeling extremely fast phenomena (on the order of sub-femtoseconds) and small-scale interactions (nanometer-level) involving large ensembles of charged particles. This makes them particularly valuable for

studying laser and beam interactions with plasmas, particularly in ultra-high-gradient particle acceleration and plasmon excitation [50].

Over the past decade, various PIC codes, for example, EPOCH [51, 52, 64], FBPIC [21, 65, 66], OSIRIS [67, 68], PIConGPU [22, 53, 69], SLIPs [70–72], Smilei [73–76], and WarpX [27, 54, 55, 77], have been extensively used to simulate laser wakefield acceleration (LWFA) and plasma wakefield acceleration (PWFA) in carbon nanostructures.

Among these codes, WarpX stands out as arguably the most comprehensive PIC code currently available. It not only incorporates the essential features of other codes but also introduces innovative functionalities, such as dynamic load balancing for CPUs and GPUs and advanced mesh refinement capabilities [55]. These features significantly improve the computational efficiency and memory usage, which is critical for large-scale simulations involving laser- and beam-plasma interactions. For example, a comparative study [78] demonstrated that WarpX achieved the lowest execution times and memory consumption among several PIC codes in 2D(3v) laser-driven ion acceleration scenarios. Although the choice of code may depend strongly on the problem being solved and the computational resources available, these performance advantages make WarpX particularly well-suited for studies involving laser- and beam-plasma interactions, which are central to our work.

For instance, Maffini et al. [77] utilized WarpX to investigate laser-driven particle acceleration within a fully ionized homogeneous carbon foam. This foam was combined with a fully ionized aluminum foil, featuring a 0.05 μm-thick ionized hydrogen layer on the rear surface to mimic contaminants. Their findings revealed that MeV protons generated through this setup could achieve particle-induced X-ray emission with performance metrics comparable to those of conventional sources. Additionally, WarpX has been widely adopted in a series of studies published throughout 2025, addressing beam-plasma and laser-plasma interactions in nanostructured media. Lei et al. [54] demonstrated that microstructured carbon nanotube forest channels can sustain ultra-high accelerating gradients exceeding 100 TeV/m, enabling compact beam-driven particle accelerators. Chu et al. [79] showed that multiple plasma channels allows controlled emission of betatron radiation from high-charge electron beams. Moreover, Lei et al. [27] found that leaky surface plasmons in nanostructured carbon nanotubes can drive efficient wakefield acceleration, offering a novel mechanism for compact accelerator design.

It is important to clarify that no internal modifications were made to the WarpX code for this study. Instead, WarpX was selected precisely because it inherently supports the simulation of complex plasma phenomena relevant to our work, including beam-plasma interaction and high-gradient acceleration.

In this work, graphene layers will be modeled as layers filled with a uniformly distributed, pre-ionized cold plasma of carbon ions and electrons. In the PIC simulations, the layers will be centered at plane $y = y_j$ with a wall thickness w_t and a volumetric density $n_{V_j} = n_{0j}/w_t$ in order to ensure that the number of free electrons within the jth layer with surface density n_{0j} in the LHM is equal to the number of free electrons in the wall thickness w_t. We will assume that the initial uniform surface electron density of each layer in the LHM can be estimated as $n_{0j} \equiv n_0 = 1.53 \times 10^{20}$ m^{-2} [80, 81], corresponding to one π electron and three σ electrons per carbon atom. Moreover, we will consider a driver proton beam with a total charge $Q = 1000e$ and a Gaussian distribution with root mean square (RMS) sizes $\sigma_x = \sigma_y = \sigma_z = 3$ nm, moving equidistantly between two graphene layers. We have chosen such a small driver

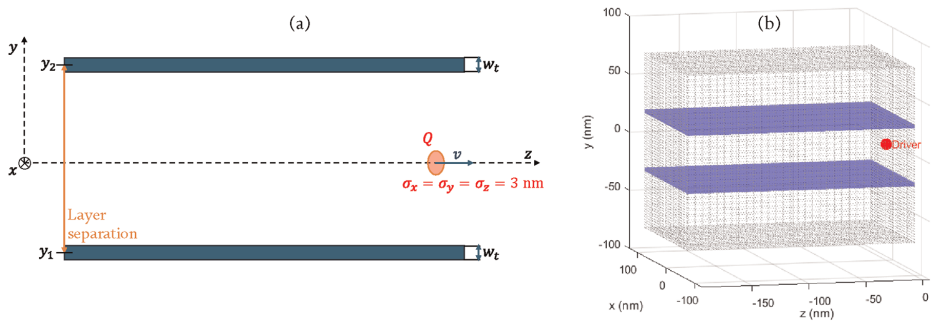

Figure 2.
(a) Scheme considered for the PIC simulations, which consists of a Gaussian proton driver beam (with RMS $\sigma_x = \sigma_y = \sigma_z$) with a total charge Q propagating along the z-axis with a velocity v. The driver beam travels between two plates, centered at y_1 and y_2, with a wall thickness w_t and a free electron volume density $n_V = n_0/w_t$. The plates are assumed to be infinitely extended in the xz-plane with a pre-ionized cold plasma of carbon ions and electrons. (b) Scheme of the meshed simulation domain indicating the driver in red and the graphene layers in blue (the mesh resolution has been reduced to $32 \times 32 \times 32$ for clearer visualization).

beam size to ensure that it can be approximated as a point-like charge, as in the LHM, since the separation between layers is considerably larger than the beam's dimensions. **Figure 2** presents a schematic representation of the simulated geometry.

The simulation domain was defined as $x_{max} = y_{max} = -x_{min} = -y_{min} = 75$ nm and $z_{min} = 2\sigma_z - 200$ nm, $z_{max} = 2\sigma_z$ with a spatial resolution of $256 \times 256 \times 256$ Yee mesh. In other words, the meshed simulation domain (in nm) is $[-75, 75] \times [-75, 75] \times [200 - \sigma_z, \sigma_z]$ with the following spatial step sizes along each axis: $\Delta x = \Delta y = 150/256$ nm and $\Delta z = 200/256$ nm (see **Figure 2(b)**). In the z-direction, a comoving window traveling at velocity v is employed, that is, moving together with the driver beam. The driver beam is initially centered at position $z = 0$, that is, close to the rear boundary z_{max} of the computational box, to ensure it remains within the domain and to accommodate the wakefield oscillations induced behind the driver within the simulation domain. The simulations span a total duration of 9.5 fs, using 5000 intermediate time steps, corresponding to a time step of 1.9 as. The choice of time step (1.9 as) was guided by the need to resolve the fastest physical processes involved in wakefield excitation, particularly the plasma oscillations and beam-plasma interactions. We verified convergence by comparing results with simulations using finer time steps, which showed negligible differences in the wakefield structure and amplitude, confirming that the chosen resolution is sufficient. At each time step, WarpX uses the finite-difference time-domain (FDTD) Yee solver to calculate the electromagnetic fields, which are then used to update the momentum and position of individual macroparticles *via* the Boris pusher implementation of the Newton–Lorentz equation. The currents generated by the electron motion are deposited onto the grid with the charge-conserving Esirkepov scheme [82], ensuring that Gauss's law remains satisfied to machine precision.

4. Results

In this section, we will compare the results obtained using the LHM with PIC simulations. We will begin by presenting the excited wakefields for a specific case in the $x\zeta$ and $y\zeta$ planes. Subsequently, we will analyze the behavior of the maximum

longitudinal wakefield excited along the z-axis as a function of the driver velocity and the separation between the graphene layers.

4.1 Excited wakefields

Figure 3 shows the longitudinal wakefield W_z, including the contribution from the driver beam, excited by a proton beam after simulating for 9.5 fs in the $y\zeta$ and $x\zeta$ planes, respectively. The wakefields generated in the vicinity of the driver beam are very intense and therefore appear saturated relative to the scale, which has been chosen to adequately observe the excitation behind the driver. It can be observed that the longitudinal wakefield induced by the presence of graphene increases in the vicinity of the graphene layers, that is, it is a plasmonic excitation. Moreover, it can be observed that the wakefields exhibit a spread in the $x\zeta$-plane (parallel to the graphene layers), which leads to a decay of the wakefield along the z-axis with increasing distance behind the driver. It is also worth mentioning that the center of the driver beam appears slightly delayed from the position where it would be expected, due to energy losses arising from its interaction with the graphene layers. For this reason, and in order to enable a direct comparison with the LHM in which energy loss is neglected, we will artificially increase the mass of the beam particles to 1 kg to mitigate the velocity loss of the driver. Furthermore, this approach enables us to subtract the wakefield generated by the driver beam by performing a simulation without plasma, thereby isolating the contribution arising solely from plasmonic excitation and allowing for a more precise comparison with the LHM.

Thus, **Figure 4** depicts the induced wakefields (after subtracting the contribution of the driver beam) in the $y\zeta$-plane and therefore does not include the wakefields generated directly by the driver itself, but rather isolates the plasmonic contribution arising from the motion of free electrons of the graphene layers. The wakefield W_x is not shown, as it is practically negligible; in fact, the LHM predicts a vanishing wakefield W_x due to symmetry considerations. A satisfactory agreement is observed between the simulation results and those provided by the LHM, particularly in the structure and amplitude of the excited wakefields in the $y\zeta$-plane, where both

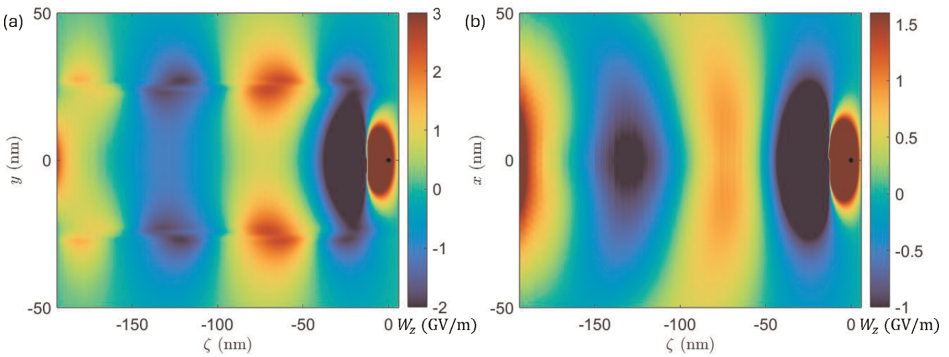

Figure 3.
*Longitudinal wakefield W_z, including the contribution from the driver beam, in the (a) $y\zeta$-plane and (b) $x\zeta$-plane for a proton beam traveling on the z-axis after simulating for 9.5 fs. The wakefields generated in the vicinity of the driver beam are significantly larger than the scale, which have been chosen to properly visualize the wakefields excited behind the driver (the same scales as in **Figure 4(a)** and **5(a)**, respectively). The black point indicates the position where the center of the beam would be located if it did not experience energy loss. We use the parameters: $v = 0.25c$, $y_2 = -y_1 = 25$ nm, $w_t = 3$ nm, $Q = 1000e$, $\sigma_x = \sigma_y = \sigma_z = 3$ nm.*

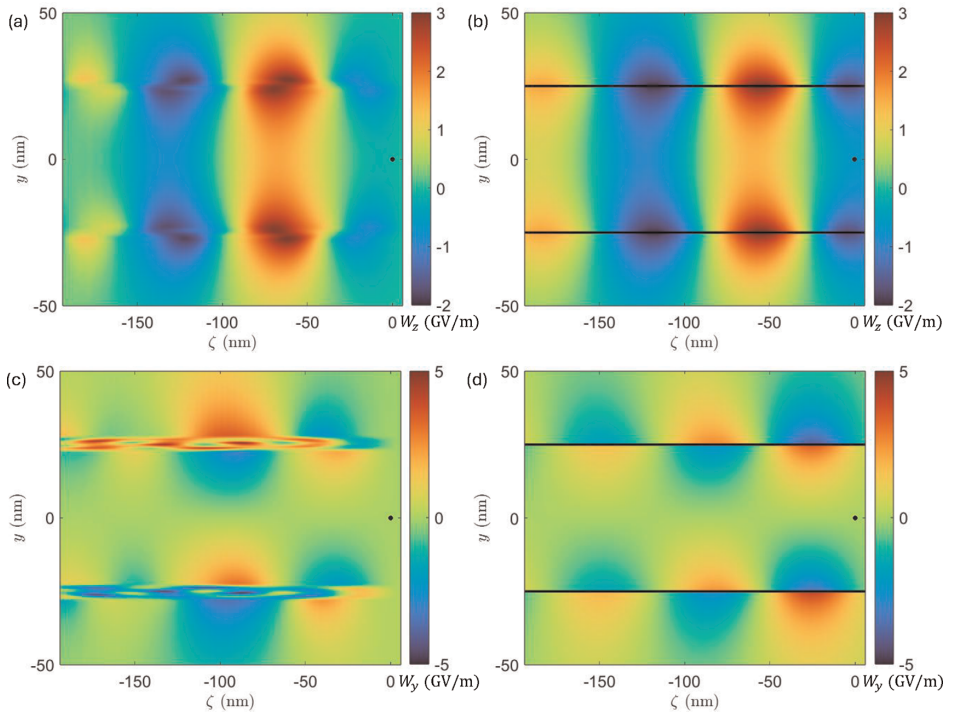

Figure 4.
*Comparison of the induced wakefields in the yζ-plane after simulating for 9.5 fs: longitudinal wakefield W_z obtained with (a) PIC simulations and (b) the LHM, and wakefield W_y obtained with (c) PIC simulations and (d) the LHM. The proton beam travels on the z-axis. In the simulations, an artificial mass of 1 kg is used for the protons in order to ensure minimal velocity loss. Therefore, we can subtract the wakefield generated by the driver beam and represent only the contribution due to plasmonic excitation, which allows for a better comparison with the LHM. The black point indicates the position of the center of the beam and the black lines the position of the graphene layers in the LHM. We use the parameters: $v = 0.25c$, $y_2 = -y_1 = 25$ nm, $w_t = 3$ nm, $Q = 1000e$, $\sigma_x = \sigma_y = \sigma_z = 3$ nm (the same as in **Figure 3**).*

approaches exhibit consistent qualitative patterns and comparable quantitative profiles. However, in the simulations, the wakefield W_y is significantly stronger within the graphene layers due to their finite thickness, an effect that cannot be captured by the LHM, which assumes infinitesimally thin sheets.

Additionally, **Figure 5** shows the induced wakefields (after subtracting the contribution of the driver beam) in the $x\zeta$-plane (parallel to the graphene layers). The wakefield W_y is not shown, as it is practically negligible; in fact, the LHM predicts a vanishing wakefield W_y due to symmetry considerations. In this case, the agreement in the longitudinal wakefield is satisfactory as well, although the LHM predicts larger absolute values in the vicinity of the driver ($\zeta \sim 0$) and in the region farther behind it ($\zeta < -150$ nm). Regarding the wakefield W_x, qualitatively similar results are obtained in both PIC simulations and the LHM; however, the quantitative agreement is not as good as in the previous cases.

Finally, **Figure 6** compares the longitudinal wakefield along the z-axis obtained from PIC simulations (both for the real proton mass and for the artificial mass of 1 kg) as well as from the LHM. In the case of the PIC simulation with the real proton mass, the field generated by the driver beam itself is taken into account. Consequently, its intensity increases drastically as we approach the driver position ($\zeta \sim 0$). In this plot,

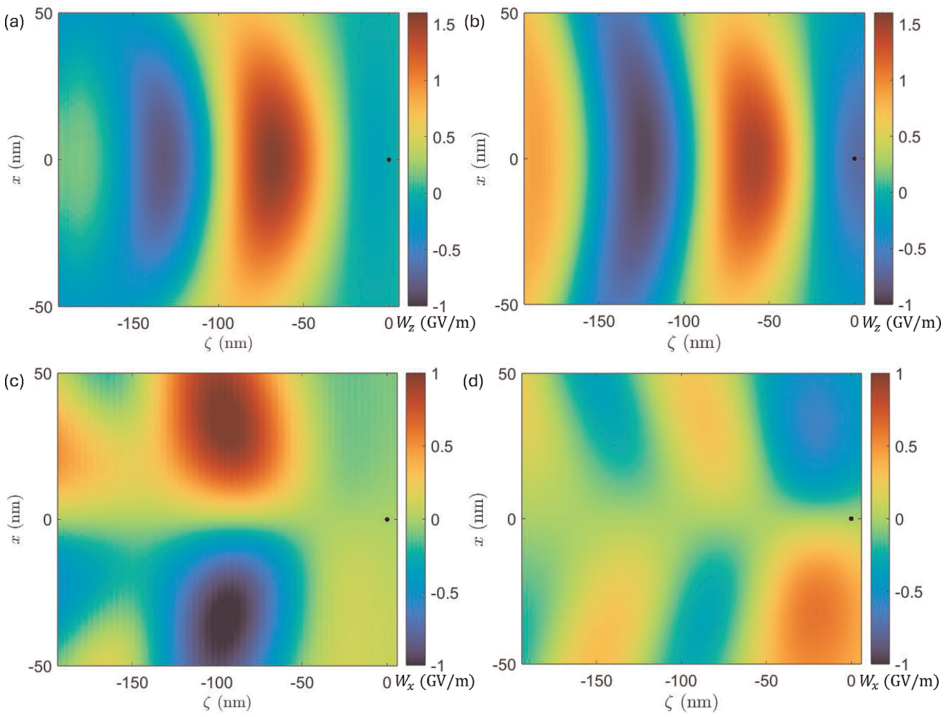

Figure 5.
*Comparison of the induced wakefields in the xζ-plane (parallel to the graphene layers) after simulating for 9.5 fs: longitudinal wakefield W_z obtained with (a) PIC simulations and (b) the LHM, and wakefield W_x obtained with (c) PIC simulations and (d) the LHM. The proton beam travels on the z-axis. In the simulations, an artificial mass of 1 kg is used for the protons in order to ensure minimal velocity loss. Therefore, we can subtract the wakefield generated by the driver beam and represent only the contribution due to plasmonic excitation, which allows for a better comparison with the LHM. The black point indicates the position of the center of the beam and the black lines the position of the graphene layers in the LHM. We use the parameters: $v = 0.25c$, $y_2 = -y_1 = 25$ nm, $w_t = 3$ nm, $Q = 1000e$, $\sigma_x = \sigma_y = \sigma_z = 3$ nm (the same as in **Figure 3**).*

it can be observed that by assigning an artificial value of 1 kg to the proton mass, a field with reduced noise is achieved. Additionally, edge effects on the left side of the plot are minimized, which are probably responsible for the increase in the wakefield, particularly evident in the simulation using the real proton mass.

4.2 Study of wakefield amplitudes

Here, we are going to study the maximum longitudinal wakefield excited along the z-axis, that is, the value of the first peak after the driver (see **Figure 6**), as a function of the separation between the graphene layers and the velocity of the driver beam.

Figure 7 presents the maximum longitudinal wakefield excited along the z-axis as a function of the separation between graphene layers $y_2 - y_1$, comparing the results of PIC simulations with those obtained using the LHM model. A good qualitative agreement can be observed between the PIC simulations and the LHM: The maximum longitudinal wakefield along the z-axis decreases as the separation between the graphene layers increases. It can be seen that, when subtracting the contribution of the driver beam, the quantitative agreement is very good; it should be recalled that the LHM refers to the induced wakefield without accounting for the beam contribution.

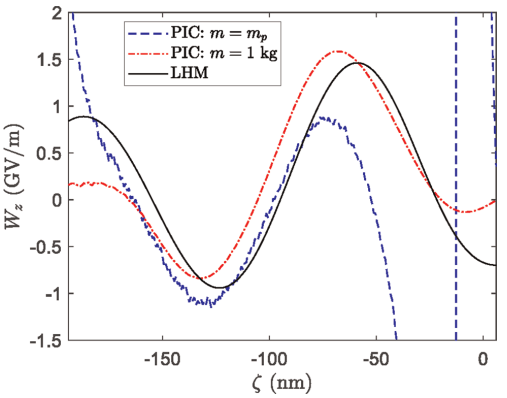

Figure 6.
*Comparison of the induced longitudinal wakefield W_z along the z-axis between PIC simulations (both for the real proton mass and for the artificial mass of 1 kg) and the LHM for a proton beam traveling on the z-axis after simulating for 9.5 fs. In the case with the real proton mass, the wakefield represents the total field, including the contribution of the driver beam. In contrast, in the other cases, this contribution has been removed to achieve a clearer visualization. We use the parameters: $v = 0.25c$, $y_2 = -y_1 = 25$ nm, $w_t = 3$ nm, $Q = 1000e$, $\sigma_x = \sigma_y = \sigma_z = 3$ nm (the same as in **Figure 3**).*

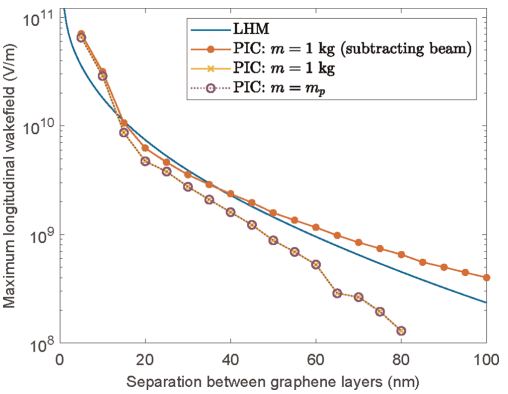

Figure 7.
Maximum longitudinal induced wakefield along the z-axis as a function of the separation between graphene layers $y_2 - y_1$ for the LHM and PIC simulations (time simulated: 9.5 fs) using the artificial mass of 1 kg and the proton mass. We use the parameters: $w_t = 3$ nm, $v = 0.25c$, $Q = 1000e$, $\sigma_x = \sigma_y = \sigma_z = 3$ nm.

Additionally, when the contribution of the driver beam is taken into account, the results are very similar for both the proton mass and the artificial mass of 1 kg. However, the agreement with the LHM worsens for large separations between the graphene layers.

On the other hand, **Figure 8** depicts the maximum longitudinal wakefield excited along the z-axis as a function of the driver velocity, comparing the results of the LHM model with those obtained from PIC simulations performed using different wall thicknesses. PIC simulations exhibit a qualitatively similar behavior to the LHM, although the maximum longitudinal wakefield is lower and the peak of the curve appears to occur at higher velocities ($\sim 0.35c$ for PIC simulations vs. $\sim 0.27c$ for the LHM). This may be influenced by the fact that, in this case, the contribution of the beam is considered in all PIC simulations. Notable differences are observed for the various wall thicknesses, particularly at low and high velocities, as well as between

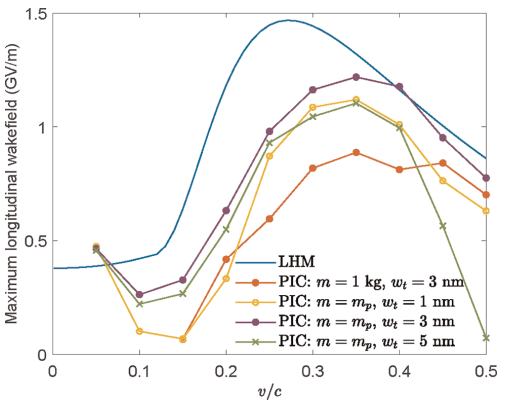

Figure 8.
Maximum longitudinal induced wakefield along the z-axis as a function of the driving velocity for the LHM and PIC simulations with different values of the wall thickness. In PIC simulations, we consider the contribution from the driver beam. We use the parameters: $y_2 = -y_1 = 25\ nm$, $Q = 1000e$, $\sigma_x = \sigma_y = \sigma_z = 3\ nm$.

simulations using the real proton mass and those employing an artificial 1 kg mass, except at low velocities $v < 0.2c$, where results are nearly identical. In general, stronger wakefields are obtained when the real proton mass is used.

5. Discussion

The differences observed between the LHM and PIC simulations stem from the distinct principles underlying each method. In the LHM framework, the driver is represented as an idealized point particle whose motion does not interact with the surrounding medium: its charge and velocity remain fixed throughout the process. In contrast, PIC simulations describe the driver as a Gaussian-shaped beam made up of many protons distributed over a finite spatial region. Additionally, since PIC simulations self-consistently account for the dynamics of all charged particles, both the driver and the surrounding medium experience mutual and self-interactions. This difference complicates direct comparisons, although certain strategies can mitigate these challenges, for example, artificially increasing the mass of the beam particles. This approach has been employed in this study, demonstrating that the use of an artificial mass allows for wakefield excitation that closely resembles the predictions of the LHM.

To achieve a meaningful comparison with the LHM, the beam size in PIC simulations must be smaller than the layer separation, necessitating a higher spatial resolution and leading to increased computational time. Moreover, a high-density beam can become susceptible to enhanced space-charge effects, altering its distribution and affecting the properties of the generated wakefields.

Another notable discrepancy stems from the absence of solid-state effects in PIC simulations. These effects, described in the LHM by parameters α, β and γ, characterize the collective behavior of electrons in graphene layers. In these layers, electron motion is facilitated along the surface, allowing for constrained yet efficient longitudinal movement. However, in PIC simulations, electrons can move freely in all directions, as no mechanisms enforce confinement to the layer. Even when collision or interaction effects are implemented through Monte Carlo Collisions (MCC) or

Fokker-Planck operators, the standard PIC solvers cannot restrict electron movement to the layer surface. In contrast, the LHM incorporates such interactions and constraints *via* the friction parameter γ.

Additionally, the comparison involves a three-dimensional volume containing free electrons, initially modeled as a thick region with a wall thickness w_t in PIC simulations, whereas the LHM considers two-dimensional surfaces with infinitesimally thin layers. Thus, while electrons and carbon ions in PIC simulations are free to move in three dimensions, in the LHM, they are confined to the surface.

Despite these methodological differences, the agreement between both approaches is satisfactory. Consequently, the LHM may serve as a valuable tool for estimating longitudinal wakefields excited in graphene layers, offering an alternative to computationally expensive PIC simulations.

6. Conclusions and outlook

In this chapter, the wakefields excited by a driver proton beam moving parallel to graphene layers have been analyzed using the LHM and compared with PIC simulations. The findings indicate that the wakefield amplitude predicted by the theoretical model aligns reasonably well with the values obtained from the simulations. The quantitative agreement improves when considering an artificial mass of 1 kg for the protons, as this minimizes velocity losses due to interactions between the beam and the surrounding medium. Additionally, we have examined the primary similarities and differences between the theoretical model and PIC simulations. Thus, the study demonstrates that the LHM provides a fast and efficient method for estimating wakefield excitation in hollow plasmas with thin walls, offering a viable alternative to computationally expensive PIC simulations.

Acknowledgements

This work has been supported by Ministerio de Universidades (Gobierno de España) under grant agreement FPU20/04958, and the Generalitat Valenciana under grant agreement CIDEGENT/2019/058.

Abbreviations

ADK	Ammosov-Delone-Krainov
DFT	density functional theory
EELS	electron energy loss spectroscopy
EPOCH	extendable particle-in-cell open collaboration
FBPIC	Fourier-Bessel particle-in-cell
FDTD	finite-difference time-domain
LHM	linearized hydrodynamic model
LWFA	laser wakefield acceleration
MCC	Monte Carlo collisions
PIC	particle-in-cell
PIConGPU	particle-in-cell on graphics processing unit
PWFA	plasma wakefield acceleration

RF	radio frequency
RMS	root mean square
RPA	random phase approximation
SLIPs	spin-resolved laser interaction with plasma simulation

Author details

Pablo Martín-Luna[1*], Juan Rodríguez-Pérez[2], Alexandre Bonatto[3], Cristian Bontoiu[4,5], Guoxing Xia[5,6] and Javier Resta-López[2,7*]

1 Instituto de Física Corpuscular (IFIC), Universitat de València - Consejo Superior de Investigaciones Científicas, Paterna, Spain

2 Instituto de Ciencia de los Materiales (ICMUV), Universitat de València, Valencia, Spain

3 Graduate Program in Information Technology and Healthcare Management, and the Beam Physics Group, Federal University of Health Sciences of Porto Alegre, Porto Alegre, RS, Brazil

4 Department of Physics, The University of Liverpool, Liverpool, United Kingdom

5 The Cockcroft Institute, Sci-Tech Daresbury, Warrington WA, United Kingdom

6 Department of Physics and Astronomy, The University of Manchester, Manchester, United Kingdom

7 Departament de Física Aplicada i Electromagnetisme, Universitat de València, Burjassot, Spain

*Address all correspondence to: pablo.martin@uv.es; javier2.resta@uv.es

IntechOpen

References

[1] Kutsaev SV. Advanced Technologies for Applied Particle Accelerators and Examples of their use (review). Technical Physics. 2021;**66**: 161-195. DOI: 10.1134/S1063784221020158

[2] Kutsaev SV. Advances in particle acceleration: Novel techniques, instruments and applications. Applied Sciences. 2024;**14**(18): 8098. DOI: 10.3390/app14188098

[3] Appleby RB, Bazzani A, Giovannozzi M, Levichev E. Focus point on high-energy accelerators: Advances, challenges, and applications. The European Physical Journal Plus. 2023; **138**(1):12. DOI: 10.1140/epjp/s13360-022-03620-8

[4] Ishikawa T. Accelerator-based X-ray sources: Synchrotron radiation, X-ray free electron lasers and beyond. Philosophical Transactions of the Royal Society A. 2019;**377**(2147): 20180231. DOI: 10.1098/rsta.2018.0231

[5] Hanna S. RF Linear Accelerators for Medical and Industrial Applications. MA, United States of America: Artech House; 2012

[6] Abe T, Kageyama T, Sakai H, Takeuchi Y, Yoshino K. Breakdown study based on direct in situ observation of inner surfaces of an RF accelerating cavity during a high-gradient test. Physical Review Accelerators and Beams. 2016;**19**:102001. DOI: 10.1103/PhysRevAccelBeams.19.102001

[7] Shao J. Investigations on RF Breakdown Phenomenon in High Gradient Accelerating Structures. Singapore: Springer; 2018. DOI: 10.1007/978-981-10-7926-9

[8] Thompson MC, Badakov H, Cook AM, Rosenzweig JB, Tikhoplav R, Travish G, et al. Breakdown limits on Gigavolt-per-meter electron-beam-driven wakefields in dielectric structures. Physical Review Letters. 2008;**100**:214801. DOI: 10.1103/PhysRevLett.100.214801

[9] Breuer J, Hommelhoff P. Laser-based acceleration of nonrelativistic electrons at a dielectric structure. Physical Review Letters. 2013;**111**:134803. DOI: 10.1103/PhysRevLett.111.134803

[10] Peralta E, Soong K, England R, Colby E, Wu Z, Montazeri B, et al. Demonstration of electron acceleration in a laser-driven dielectric microstructure. Nature. 2013;**503**(7474): 91-94. DOI: 10.1038/nature12664

[11] England RJ, Noble RJ, Bane K, Dowell DH, Ng CK, Spencer JE, et al. Dielectric laser accelerators. Reviews of Modern Physics. 2014;**86**:1337-1389. DOI: 10.1103/RevModPhys.86.1337

[12] O'Shea B, Andonian G, Barber S, Fitzmorris K, Hakimi S, Harrison J, et al. Observation of acceleration and deceleration in gigaelectron-volt-per-metre gradient dielectric wakefield accelerators. Nature communications. 2016;**7**(1):1-7. DOI: 10.1038/ncomms12763

[13] Tajima T, Dawson JM. Laser electron accelerator. Physical Review Letters. 1979;**43**:267-270. DOI: 10.1103/PhysRevLett.43.267

[14] Chen P, Dawson JM, Huff RW, Katsouleas T. Acceleration of electrons by the interaction of a bunched electron beam with a plasma. Physical Review Letters. 1985;**54**:693-696. DOI: 10.1103/PhysRevLett.54.693

[15] Maffini A, Mirani F, Galbiati M, Ambrogioni K, Gatti F, Galli De Magistris MS, et al. Towards compact laser-driven accelerators: Exploring the potential of advanced double-layer targets. EPJ Techniques and Instrumentation. 2023;**10**:15. DOI: 10.1140/epjti/s40485-023-00102-8

[16] Leemans WP, Nagler B, Gonsalves AJ, Tóth C, Nakamura K, Geddes CG, et al. GeV electron beams from a centimetre-scale accelerator. Nature physics. 2006;**2**(10):696-699. DOI: 10.1038/nphys418

[17] Litos M, Adli E, An W, Clarke C, Clayton C, Corde S, et al. High-efficiency acceleration of an electron beam in a plasma Wakefield accelerator. Nature. 2014;**515**(7525):92-95. DOI: 10.1038/nature13882

[18] Tajima T, Cavenago M. Crystal x-ray accelerator. Physical Review Letters. 1987;**59**:1440-1443. DOI: 10.1103/PhysRevLett.59.1440

[19] Chen P, Noble RJ. A solid state accelerator. In: AIP Conf. Proc. Vol. 156. New York: AIP; 1987. pp. 222-227. DOI: 10.1063/1.36458

[20] Chen P, Noble RJ. Crystal channel collider: Ultra-high energy and luminosity in the next century. In: AIP Conf. Proc. Vol. 398. New York: AIP; 1997. pp. 273-285. DOI: 10.1063/1.53055

[21] Bonatto A, Xia G, Apsimon O, Bontoiu C, Kukstas E, Rodin V, et al. Exploring ultra-high-intensity wakefields in carbon nanotube arrays: An effective plasma-density approach. Physics of Plasmas. 2023;**30**(3):033105. Available from:. DOI: 10.1063/5.0134960

[22] Bonțoiu C, Apsimon O, Kukstas E, Rodin V, Yadav M, Welsch C, et al. TeV/m catapult acceleration of electrons in graphene layers. Scientific Reports. 2023;**13**:1330. DOI: 10.1038/s41598-023-28617-w

[23] Martín-Luna P, Bonatto A, Bontoiu C, Xia G, Resta-López J. Excitation of wakefields in carbon nanotubes: A hydrodynamic model approach. New Journal of Physics. 2023;**25**(12):123029. DOI: 10.1088/1367-2630/ad127c

[24] Martín-Luna P, Bonatto A, Bontoiu C, Xia G, Resta-López J. Plasmonic excitations in double-walled carbon nanotubes. Results in Physics. 2024;**60**:107698. DOI: 10.1016/j.rinp.2024.107698

[25] Martín-Luna P, Bonatto A, Bontoiu C, Lei B, Xia G, Resta-López J. Wakefield excitation and stopping power in multi-walled carbon nanotubes: One- and two-fluid model. Journal of Physics D: Applied Physics. 2025;**58**(22):225203. DOI: 10.1088/1361-6463/add545

[26] Martín-Luna P, Bonatto A, Bontoiu C, Lei B, Xia G, Resta-López J. Plasmonic excitations in graphene layers. Chinese Journal of Physics. 2025;**97**:607-624. DOI: 10.1016/j.cjph.2025.03.030

[27] Lei B, Zhang H, Bonțoiu C, Bonatto A, Martín-Luna P, Liu B, et al. Leaky surface plasmon-based wakefield acceleration in nanostructured carbon nanotubes. Plasma Physics and Controlled Fusion. 2025;**67**(6):065036. DOI: 10.1088/1361-6587/ade00a

[28] Novoselov KS, Geim AK, Morozov SV, Jiang D, Zhang Y, Dubonos SV, et al. Electric field effect in atomically thin carbon films. Science. 2004;**306**(5696):666-669. DOI: 10.1126/science.1102896

[29] Luo X, Qiu T, Lu W, Ni Z. Plasmons in graphene: Recent progress and applications. Materials Science and Engineering: R: Reports. 2013;**74**(11): 351-376. DOI: 10.1016/j.mser.2013.09.001

[30] Yan JA, Ruan WY, Chou MY. Phonon dispersions and vibrational properties of monolayer, bilayer, and trilayer graphene: Density-functional perturbation theory. Physical Review B. 2008;**77**:125401. DOI: 10.1103/PhysRevB.77.125401

[31] Wang H, Wang Y, Cao X, Feng M, Lan G. Vibrational properties of graphene and graphene layers. Journal of Raman Spectroscopy: An International Journal for Original Work in all Aspects of Raman Spectroscopy, Including Higher Order Processes, and also Brillouin and Rayleigh Scattering. 2009; **40**(12):1791-1796. DOI: 10.1002/jrs.2321

[32] Cooper DR, D'Anjou B, Ghattamaneni N, Harack B, Hilke M, Horth A, et al. Experimental review of graphene. International Scholarly Research Notices. 2012;**2012**(1):501686. DOI: 10.5402/2012/501686

[33] Nilsson J, Neto AHC, Guinea F, Peres NMR. Electronic properties of graphene multilayers. Physical Review Letters. 2006;**97**:266801. DOI: 10.1103/PhysRevLett.97.266801

[34] Novoselov KS, Morozov SV, Mohinddin TMG, Ponomarenko LA, Elias DC, Yang R, et al. Electronic properties of graphene. Physica Status Solidi (b). 2007;**244**(11):4106-4111. DOI: 10.1002/pssb.200776208

[35] Castro Neto AH, Guinea F, Peres NMR, Novoselov KS, Geim AK. The electronic properties of graphene. Reviews of Modern Physics. 2009;**81**:109-162. DOI: 10.1103/RevModPhys.81.109

[36] Radović I, Borka D. Wake effect in interactions of fast ions with supported two-dimensional electron gas. Nuclear Instruments and Methods in Physics Research Section B: Beam Interactions with Materials and Atoms. 2010;**268**(17): 2649-2654. DOI: 10.1016/j.nimb.2010.06.043

[37] Kinyanjui MK, Kramberger C, Pichler T, Meyer JC, Wachsmuth P, Benner G, et al. Direct probe of linearly dispersing 2D interband plasmons in a free-standing graphene monolayer. Europhysics Letters. 2012;**97**(5):57005. DOI: 10.1209/0295-5075/97/57005

[38] Wachsmuth P, Hambach R, Kinyanjui MK, Guzzo M, Benner G, Kaiser U. High-energy collective electronic excitations in free-standing single-layer graphene. Physical Review B. 2013;**88**:075433. DOI: 10.1103/PhysRevB.88.075433

[39] Eberlein T, Bangert U, Nair RR, Jones R, Gass M, Bleloch AL, et al. Plasmon spectroscopy of free-standing graphene films. Physical Review B. 2008; **77**:233406. DOI: 10.1103/PhysRevB.77.233406

[40] Fermanian Kammerer C, Méhats F. A kinetic model for the transport of electrons in a graphene layer. Journal of Computational Physics. 2016;**327**: 450-483. DOI: 10.1016/j.jcp.2016.09.010

[41] Allison KF, Borka D, Radović I, Hadžievski L, Mišković ZL. Dynamic polarization of graphene by moving external charges: Random phase approximation. Physical Review B. 2009; **80**:195405. DOI: 10.1103/PhysRevB.80.195405

[42] Loche P, Ayaz C, Schlaich A, Bonthuis DJ, Netz RR. Breakdown of linear dielectric theory for the interaction between hydrated ions and

graphene. The Journal of Physical Chemistry Letters. 2018;**9**(22): 6463-6468. DOI: 10.1021/acs.jpclett.8b02473

[43] Radović I, Hadžievski L, Bibić N, Mišković ZL. Dynamic-polarization forces on fast ions and molecules moving over supported graphene. Physical Review A—Atomic, Molecular, and Optical Physics. 2007;**76**(4):042901. DOI: 10.1103/PhysRevA.76.042901

[44] Radović I, Borka D. Interactions of fast charged particles with supported two-dimensional electron gas: One-fluid model. Physics Letters A. 2010;**374**(13): 1527-1533. DOI: 10.1016/j.physleta.2010.01.056

[45] Li CZ, Wang YN, Song YH, Mišković ZL. Interactions of charged particle beams with double-layered two-dimensional quantum electron gases. Physics Letters A. 2014;**378**(22): 1626-1631. DOI: 10.1016/j.physleta.2014.04.007

[46] Borka D, Radović I, Vuković K. Energy loss of charged particles traversing multilayer graphene. Nuclear Instruments and Methods in Physics Research Section B: Beam Interactions with Materials and Atoms. 2015;**347**: 7-10. DOI: 10.1016/j.nimb.2015.01.057

[47] Chaves AJ, Peres NMR, Smirnov G, Mortensen NA. Hydrodynamic model approach to the formation of plasmonic wakes in graphene. Physical Review B. 2017;**96**:195438. DOI: 10.1103/PhysRevB.96.195438

[48] Polini M, Tomadin A, Asgari R, MacDonald AH. Density functional theory of graphene sheets. Physical Review B. 2008;**78**:115426. DOI: 10.1103/PhysRevB.78.115426

[49] Xq S, Zhang H, Xl C, Miyamoto Y. Tunable plasmons in few-layer nitrogen-doped graphene nanostructures: A time-dependent density functional theory study. Physical Review B. 2016;**93**: 195424. DOI: 10.1103/PhysRevB.93.195424

[50] Ding WJ, Lim JZJ, Do HTB, Xiong X, Mahfoud Z, Png CE, et al. Particle simulation of plasmons. Nano. 2020; **9**(10):3303-3313. DOI: 10.1515/nanoph-2020-0067

[51] Sangwan D, Culfa O, Ridgers CP, Aogaki S, Stutman D, Diaconescu B. Simulations of carbon ion acceleration by 10 PW laser pulses on ELI-NP. Laser and Particle Beams. 2019;**37**(4):346-353. DOI: 10.1017/S0263034619000648

[52] Arber TD, Bennett K, Brady CS, Lawrence-Douglas A, Ramsay MG, Sircombe NJ, et al. Contemporary particle-in-cell approach to laser-plasma modelling. Plasma Physics and Controlled Fusion. 2015;**57**(11):113001. DOI: 10.1088/0741-3335/57/11/113001

[53] Bussmann M, Burau H, Cowan TE, Debus A, Huebl A, Juckeland G, et al. Radiative signatures of the relativistic kelvin-Helmholtz instability. In: Proceedings of the International Conference on High Performance Computing, Networking, Storage and Analysis. SC'13. New York, NY, USA: Association for Computing Machinery; 2013. DOI: 10.1145/2503210.2504564

[54] Lei B, Zhang H, Bonțoiu C, Bonatto A, Resta-López J, Xia G, et al. 100s TeV/m-level particle accelerators driven by high-density electron beams in micro structured carbon nanotube forest channel. New Journal of Physics. 2025; **27**(8):084301. DOI: 10.1088/1367-2630/adf87d

[55] Fedeli L, Huebl A, Boillod-Cerneux F, Clark T, Gott K, Hillairet C, et al. Pushing the Frontier in the design of

laser-based electron accelerators with groundbreaking mesh-refined particle-in-cell simulations on exascale-class supercomputers. In: SC22: International Conference for High Performance Computing, Networking, Storage and Analysis. Dallas, Texas, USA: IEEE; 2022. pp. 1-12. DOI: 10.1109/SC41404.2022.00008

[56] Ciracì C, Pendry JB, Smith DR. Hydrodynamic model for plasmonics: A macroscopic approach to a microscopic problem. ChemPhysChem. 2013;**14**(6):1109-1116. DOI: 10.1002/cphc.201200992

[57] Toscano G, Straubel J, Kwiatkowski A, Rockstuhl C, Evers F, Xu H, et al. Resonance shifts and spill-out effects in self-consistent hydrodynamic nanoplasmonics. Nature Communications. 2015;**6**(1):7132. DOI: 10.1038/ncomms8132

[58] Hakimi S, Nguyen T, Farinella D, Lau CK, Wang HY, Taborek P, et al. Wakefield in solid state plasma with the ionic lattice force. Physics of Plasmas. 2018;**25**(2):023112. DOI: 10.1063/1.5016445

[59] Hakimi S, Zhang X, Lau C, Taborek P, Dollar F, Tajima T. X-ray laser Wakefield acceleration in a nanotube. International Journal of Modern Physics A. 2019;**34**(34):1943011. DOI: 10.1142/S0217751X19430115

[60] Nejati M, Javaherian C, Shokri B, Jazi B. The single-wall carbon nanotube waveguides and excitation of their $\sigma + \pi$ plasmons by an electron beam. Physics of Plasmas. 2009;**16**(2):022108. DOI: 10.1063/1.3077306

[61] Arista NR. Interaction of ions and molecules with surface modes in cylindrical channels in solids. Physical Review A. 2001;**64**:032901. DOI: 10.1103/PhysRevA.64.032901

[62] Ammosov MV, Delone NB, Krainov VP. Tunnel ionization of complex atoms and of atomic ions in an alternating electromagnetic field. Soviet. Journal of Experimental and Theoretical Physics. 1986;**64**(6):1191. DOI: 10.1117/12.938695

[63] Chen M, Cormier-Michel E, Geddes CGR, Bruhwiler DL, Yu LL, Esarey E, et al. Numerical modeling of laser tunneling ionization in explicit particle-in-cell codes. Journal of Computational Physics. 2013;**236**:220-228. DOI: 10.1016/j.jcp.2012.11.029

[64] Zhang X, Tajima T, Farinella D, Shin Y, Mourou G, Wheeler J, et al. Particle-in-cell simulation of x-ray Wakefield acceleration and betatron radiation in nanotubes. Physical Review Accelerators and Beams. 2016;**19**:101004. DOI: 10.1103/PhysRevAccelBeams.19.101004

[65] Lehe R, Kirchen M, Andriyash IA, Godfrey BB, Vay JL. A spectral, quasi-cylindrical and dispersion-free particle-in-cell algorithm. Computer Physics Communications. 2016;**203**:66-82. DOI: 10.1016/j.cpc.2016.02.007

[66] Martín-Luna P, Bonatto A, Bontoiu C, Xia G, Resta-López J. Plasmonic excitations in carbon nanotubes: PIC simulations vs hydrodynamic model. In: Baccouch M, editor. Computational Fluid Dynamics. Rijeka: IntechOpen; 2024. DOI: 10.5772/intechopen.1006820

[67] Fonseca RA, Silva LO, Tsung FS, Decyk VK, Lu W, Ren C, et al. OSIRIS: A three-dimensional, fully relativistic particle in cell code for Modeling plasma based accelerators. In: Sloot PMA,

Hoekstra AG, Tan CJK, Dongarra JJ, editors. Computational Science — ICCS 2002. Berlin, Heidelberg: Springer Berlin Heidelberg; 2002. pp. 342-351. DOI: 10.1007/3-540-47789-6_36

[68] Dover NP, Najmudin Z. Ion acceleration in the radiation pressure regime with ultrashort pulse lasers. High Energy Density Physics. 2012;**8**(2): 170-174. DOI: 10.1016/j.hedp.2012.02.002

[69] Sharma A, Kamperidis C. High energy proton micro-bunches from a laser plasma accelerator. Scientific Reports. 2019;**9**(13840):13840. DOI: 10.1038/s41598-019-50348-0

[70] Wan F, Lv C, Xue K, Dou ZK, Zhao Q, Ababekri M, et al. Simulations of spin/polarization-resolved laser–plasma interactions in the nonlinear QED regime. Matter and Radiation at Extremes. 2023;**8**(6):064002. DOI: 10.1063/5.0163929

[71] Xue K, Sun T, Wei KJ, Li ZP, Zhao Q, Wan F, et al. Generation of high-density high-polarization positrons via single-shot strong laser-foil interaction. Physical Review Letters. 2023;**131**:175101. DOI: 10.1103/PhysRevLett.131.175101

[72] Dou ZK, Lv C, Salamin YI, Zhang N, Wan F, Xu ZF, et al. Compact spin-polarized positron acceleration in multilayer microhole-array films. Physical Review E. 2025;**111**:035209. DOI: 10.1103/PhysRevE.111.035209

[73] Derouillat J, Beck A, Pérez F, Vinci T, Chiaramello M, Grassi A, et al. Smilei : A collaborative, open-source, multi-purpose particle-in-cell code for plasma simulation. Computer Physics Communications. 2018;**222**:351-373. DOI: 10.1016/j.cpc.2017.09.024

[74] Heppe C, Kumar N. High brilliance γ-ray generation from the laser interaction in a carbon plasma channel. Frontiers in Physics. 2022;**10**:987830. DOI: 10.3389/fphy.2022.987830

[75] Azamoum Y, Becker GA, Keppler S, Duchateau G, Skupin S, Grech M, et al. Optical probing of ultrafast laser-induced solid-to-overdense-plasma transitions. Light: Science Applications. 2024;**13**:109. DOI: 10.1038/s41377-024-01444-y

[76] Pan Z, Liu J, Wang P, Mei Z, Cao Z, Kong D, et al. Electron acceleration and x-ray generation from near-critical-density carbon nanotube foams driven by moderately relativistic lasers. Physics of Plasmas. 2024;**31**(4):043108. DOI: 10.1063/5.0202843

[77] Maffini A, Mirani F, Galbiati M, Ambrogioni K, Gatti F, Galli De Magistris MS, et al. Towards compact laser-driven accelerators: Exploring the potential of advanced double-layer targets. EPJ Techniques and Instrumentation. 2023;**10**:15. DOI: 10.1140/epjti/s40485-023-00102-8

[78] Smith JR, Orban C, Rahman N, McHugh B, Oropeza R, Chowdhury EA. A particle-in-cell code comparison for ion acceleration: EPOCH, LSP, and WarpX. Physics of Plasmas. 2021;**28**(7): 074505. DOI: 10.1063/5.0053109

[79] Chu M, Luan S, Yang H, Feng K, Tian Y, Yang X, et al. Controlled betatron radiation from high-charge electron beams in multiple plasma channels. Optics Express. 2025;**33**(10):21070-21078. DOI: 10.1364/OE.557855

[80] Östling D, Tománek D, Rosén A. Electronic structure of single-wall, multiwall, and filled carbon nanotubes. Physical Review B. 1997;**55**:13980-13988. DOI: 10.1103/PhysRevB.55.13980

[81] Mowbray DJ, Mišković ZL, Goodman FO, Wang YN. Interactions of fast ions with carbon nanotubes: Two-fluid model. Physical Review B. 2004;**70**: 195418. DOI: 10.1103/PhysRevB.70.195418

[82] Esirkepov TZ. Exact charge conservation scheme for particle-in-cell simulation with an arbitrary form-factor. Computer Physics Communications. 2001;**135**(2):144-153. DOI: 10.1016/S0010-4655(00)00228-9